Spin waves throughout the Brillouin zone and magnetic exchange coupling in the ferromagnetic metallic manganites $La_{1-x}Ca_xMnO_3$ $(x=0.25,0.30)$

F. Ye,[1,*] Pengcheng Dai,[2,1] J. A. Fernandez-Baca,[1,2] D. T. Adroja,[3] T. G. Perring,[3] Y. Tomioka,[4] and Y. Tokura[4,5]
[1]*Neutron Scattering Science Division, Oak Ridge National Laboratory, Oak Ridge, Tennessee 37831-6393, USA*
[2]*Department of Physics and Astronomy, The University of Tennessee, Knoxville, Tennessee 37996-1200, USA*
[3]*ISIS Facility, Rutherford Appleton Laboratory, Chilton, Didcot OX11 0QX, United Kingdom*
[4]*Correlated Electron Research Center (CERC), Tsukuba 305-0046, Japan*
[5]*Department of Applied Physics, University of Tokyo, Tokyo 113-8656, Japan*
(Received 22 December 2006; revised manuscript received 5 February 2007; published 6 April 2007)

Using time-of-flight and triple-axis inelastic neutron spectroscopy, we determine spin-wave excitations throughout the Brillouin zone for ferromagnetic manganites $La_{1-x}Ca_xMnO_3$ $(x=0.25,0.3)$ in their low-temperature metallic states. While spin-wave excitations in the long-wavelength limit (spin stiffness D) have similar values for both compounds, the excitations near the Brillouin-zone boundary of $La_{0.7}Ca_{0.3}MnO_3$ are considerably softened in all symmetry directions compared to that of $La_{0.75}Ca_{0.25}MnO_3$. A Heisenberg model with the nearest neighbor and the fourth neighbor exchange interactions can describe the overall dispersion curves fairly well. We compare the data with various theoretical models describing the spin excitations of ferromagnetic manganites.

DOI: 10.1103/PhysRevB.75.144408 PACS number(s): 75.30.Ds, 61.12.−q, 71.30.+h, 72.15.Gd

I. INTRODUCTION

The experimental investigation of spin dynamical properties in doped manganese perovskite $A_{1-x}B_xMnO_3$, where A is the trivalent ion (La^{3+}, Pr^{3+}, Nd^{3+}, etc.) and B is the divalent ion (Ca^{2+} or Sr^{2+}), is essential to the understanding of spin-spin interactions in these materials. At hole-doping level $x \approx 0.30$, these so-called colossal magnetoresistance (CMR) compounds exhibit an unusually large change in electrical resistance in response to a magnetic field and changes from a paramagnetic to a ferromagnetic state.[1–3] The Mn $3d$ levels in the Mn^{3+}/Mn^{4+} mixed valent system, split by the oxygen octahedral crystal field to a lower-energy t_{2g} triplet and a higher-energy e_g doublet, are filled according to Hund's rule such that all spins are aligned on a given site by a large intra-atomic exchange coupling J_H. The basic microscopic mechanism responsible for the CMR effect is the double-exchange (DE) interaction,[4] where ferromagnetism and electrical conductivity arise from hopping of the itinerant e_g electrons with kinetic energy t from trivalent Mn^{3+} to tetravalent Mn^{4+} sites. In its simplest form, the Hamiltonian of a DE model can be described as a single band of itinerant e_g electrons interacting with localized core spins by Hund's rule exchange J_H. Since J_H is much larger than t, the kinetic energy of itinerant e_g electrons is minimal when all electron spins are parallel; i.e., the ground state is a metallic ferromagnet.

Although DE interaction is believed to be responsible for the ferromagnetism and electron conductivity in CMR compounds, whether the magnetic excitations of such a model can be discussed in terms of an equivalent ferromagnetic Heisenberg model is still not clear. In the strong coupling limit $(t/J_H \rightarrow 0)$, Furukawa[5] has shown that the DE model can be mapped onto the Heisenberg Hamiltonian with only the nearest-neighbor (NN) exchange coupling. In this scenario, the magnitude of the exchange coupling J associated with ferromagnetic spin waves should scale with the Curie temperature T_C, kinetic energy t, and doping x.[6–9] Experimentally, the initial measurements on $La_{0.7}Pb_{0.3}MnO_3$ suggest that a simple NN Heisenberg model is sufficient to account for the entire spin-wave dispersion relation[7] and the exchange coupling obtained from such model also yields, to within 15%, the correct T_C of the compound. However, later experimental measurements indicate that spin-wave excitations of most $A_{1-x}B_xMnO_3$ manganites with $x \approx 0.3$ renormalize near the zone boundary (ZB) with large softening and damping.[10–14] Furthermore, the spin-wave stiffness constant D and the NN magnetic exchange coupling J are weakly dependent on T_C and doping level x in metallic ferromagnetic (FM) manganites.[15–17]

It is now well established that a Heisenberg model with NN exchange coupling is insufficient to describe the dispersion relation of CMR manganites; several possible microscopic mechanisms have been proposed to address the unusual features of spin-wave excitations near the ZB. First, realistic calculations based on the DE mechanism with consideration of the finite kinetic energy t and the effect of on-site Coulomb repulsion show that spin waves in the DE model do not map to the Heisenberg Hamiltonian with simple NN exchange coupling.[18] This model, however, predicts a doping dependence on D which is not observed experimentally. Second, the observed ZB spin-wave softening may be due to the conduction electron band filling effect, where the existence of long-range magnetic interactions leads to the softening at the ZB.[19] On the other hand, whether this approach is capable of explaining the observed spin-wave broadening remains unclear. Third, large magnon-phonon interactions may give rise to the remarkable ZB softening along specific directions.[12] Fourth, the deviation of short-wavelength magnons from the canonical Heisenberg form might originate from the scattering of magnons by collective quantum orbital fluctuations, which could either be planar (x^2-y^2)-type orbitals associated with the A-type antiferromagnetic (AF) ordering[20,21] or rodlike $(3z^2-r^2)$ orbital

correlations related to *C*-type AF ordering.[22] Depending on the actual orbital shape, the coupling between charge and orbital lattice will give rise to distinct doping dependence of the softening and/or broadening of the magnetic spectrum. Fifth, the randomness created by the substitution of the divalent ions for the trivalent ions in $A_{1-x}B_xMnO_3$ might be responsible for the anomalous spin-wave softening.[23,24] Finally, the overlap between the magnon excitations and Stoner continuum in the metallic $A_{1-x}B_xMnO_3$ would cause softening and broadening of the magnon branch near ZB.[25,26] Although this single-band DE model with intermediate coupling can explain the softening and/or broadening in the low-T_C compounds, remarkable similarities in systems with widely different T_C's indicate that it is inadequate as the bandwidth of Stoner continuum is directly related to the T_C's.

Given that there are so many possible models to explain the ZB magnon softening, it is imperative to carry out systematic spin-wave measurements and compare the results with predictions of various models. In a recent letter,[17] we made such comparison for spin waves along the $[\xi,0,0]$ direction and found that none of the prevailing models can account for the data. In this paper, we expand our previous work and describe a systematic investigation of spin-wave excitations of the CMR manganites $La_{0.75}Ca_{0.25}MnO_3$ (LCMO25) and $La_{0.70}Ca_{0.30}MnO_3$ (LCMO30). Using reactor based and time-of-flight inelastic-neutron-scattering (INS) techniques, we were able to map out the low-temperature ferromagnetic spin-wave excitations of LCMO25 and LCMO30 throughout the Brillouin zone in all symmetry directions. In the long-wavelength limit, spin-wave stiffness of LCMO25 and LCMO30 are 147±3 and 169±2 meV Å^2, respectively, consistent with previous results.[16,17] At large wave vectors, we find that the dispersion relations of LCMO30 are considerably more renormalized (softened) in all major symmetry directions compared to those of LCMO25. The softening is well described by the introduction of the fourth NN ferromagnetic exchange coupling J_4 [Fig. 1(b)]; the ratio of J_4/J_1 is about 19.5% in LCMO30 and 6.5% in LCMO25. In Sec. II, we describe the experimental details. Section III gives the data analysis and comparison with previous work. The conclusions are summarized in Sec. IV.

II. EXPERIMENTAL DETAILS

We grew single crystals of LCMO25 and LCMO30 using the traveling solvent floating zone technique. The Curie temperatures of LCMO25 (T_C=190±1 K) and LCMO30 (T_C=238±1 K) are determined from the elastic neutron diffraction on the (100) and (110) magnetic Bragg peaks.[27] LCMO25 has a nominal hole-doping level of x=0.25, just above the metal-insulator transition concentration (x=0.22). LCMO30 has a doping level close to optimal doping with highest T_C. Our INS experiments were performed on the high-energy transfer (HET) chopper spectrometer at the ISIS spallation neutron source, Rutherford Appleton Laboratory, and on the HB1/HB3 triple-axis spectrometers at the high-flux-isotope reactor (HFIR), Oak Ridge National Laboratory.

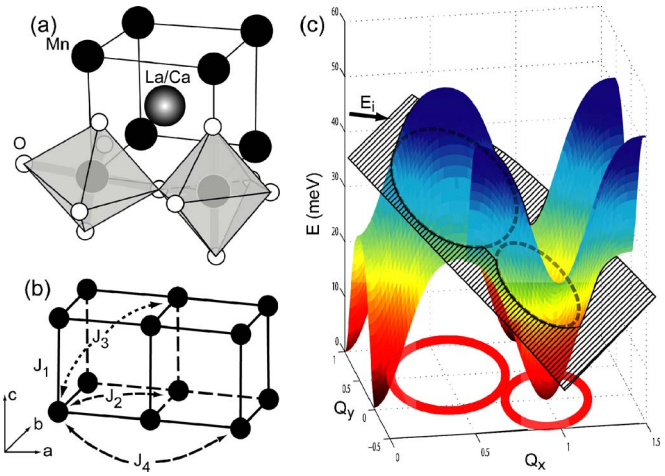

FIG. 1. (Color online) (a) Crystal structure of $La_{1-x}Ca_xMnO_3$ with distorted oxygen octahedra surrounding Mn ions. (b) Magnetic exchange interactions up to fourth-order between adjacent Mn ions. (c) Illustration of time-of-flight experiment. The energy–wave-vector (E-q) region probed by the experiment intersects the spin-wave dispersion surface, giving rise to spin-wave rings projected on the scattering plane. For smaller energy transfer E, the ring centers at the zone center. For larger E, the ring centers at the ZB.

The momentum transfer wave vectors $q=(q_x,q_y,q_z)$ are in units of Å^{-1} at positions $(H,K,L)=(q_xa/2\pi,q_yb/2\pi, q_zc/2\pi)$ in reciprocal lattice units (rlu), where $a\approx b\approx c \approx 3.87$ Å and 3.86 Å are the lattice parameters of the pseudocubic unit cells of LCMO25 and LCMO30, respectively [Fig. 1(a)]. The samples were aligned in the (H,H,L) zone in both the ISIS and HFIR experiments. For the ISIS measurements, we use the HET direct-geometry chopper spectrometer which has the ^{3}He-filled detector tubes covering the scattering angles from 9°–29° [position sensitive detectors (PSD) cover from 2.5°–7.9°]. For the HFIR experiment, we use pyrolytic graphite as monochromator, analyzer, and filters, and the final neutron energy was fixed at E_f =13.5 or 14.7 meV.

For the HET measurements, the magnetic scattering intensities of the raw data were normalized to a vanadium standard. The scattering function

$$S(\mathbf{q},\omega)=\frac{|k_i|}{|k_f|}\frac{d^2\sigma}{d\Omega\, d\omega}, \tag{1}$$

where k_i and k_f are the initial and final neutron wave vectors, respectively, the solid angle of scattering is Ω, and the energy transfer is $\hbar\omega$. We used the program MSLICE (Ref. 28) to visualize the $\mathbf{q}$-ω data sets and to prepare the one-dimensional cuts along the high-symmetry spin-wave directions needed for further analysis using the program TOBYFIT.[29]

III. MODELING AND ANALYSIS

The neutron-scattering cross section per f.u. for spin-wave excitations is

$$\frac{d^2\sigma}{d^2\Omega\, d\omega} = (\gamma r_0)^2 \frac{|k_f|}{|k_i|} |F(\mathbf{q})|^2 \frac{1}{\pi g^2 \mu_B^2} \frac{1}{1 - e^{-\beta\hbar\omega}} \chi''(\mathbf{q},\omega), \tag{2}$$

where $(\gamma r_0)^2 = 0.2906$ b, $|F(\mathbf{q})|^2$ is the magnetic form factor, g is the Lande factor (≈ 2), $[n(\omega)+1] = 1/[1 - \exp(-\hbar\omega/k_B T)]$ is the detailed balance factor, and μ_B is the Bohr magneton. $\chi''(\mathbf{q},\omega)$ is the imaginary part of the generalized spin susceptibility which depends on the wave vector q and energy transfer $\hbar\omega$. In the damped simple harmonic oscillator (DSHO) approximation, the normalized dynamical susceptibility $\chi''(\mathbf{q},\omega)$ can be written as

$$\chi''(\mathbf{q},\omega) = \frac{4\gamma\omega\omega_0}{\pi[(\omega^2 - \omega_0^2)^2 + 4(\gamma\omega)^2]}, \tag{3}$$

where γ characterizes the damping of the magnetic spins and ω_0 is directly associated with the spin-wave dispersion relation. In the light damping limit, the intrinsic peak height A and width Γ of the spin-wave excitation profiles are determined by the damping γ and become

$$A \propto 1/(2\pi\gamma), \quad \Gamma \propto 2\gamma. \tag{4}$$

The Hamiltonian for a Heisenberg ferromagnet is

$$H = -\frac{1}{2}\sum_{i,k} J_k \mathbf{S}_i \cdot \mathbf{S}_{i+k}, \tag{5}$$

where $\mathbf{S}_i$ denotes the magnetic moment at site i and J_k indicates the magnetic exchange coupling between neighboring sites. In an early study, a NN coupling J_1 has been successfully employed to describe the entire spin-wave dispersion relation $E(\mathbf{q})$ for high-T_C manganites.[7] Subsequent measurements have shown the presence of ZB spin-wave softening for all other manganites with dispersions being reproduced well by a Heisenberg Hamiltonian with higher-order interactions.[10,17,22] Recently, we found that the introduction of the fourth NN interactions J_4 gives a satisfactory description of ZB softening of the spin-wave dispersions for a wide range of doped manganites along the $[\xi,0,0]$ direction.[17] We show here that such model also gives reasonable description of spin waves in all other symmetry directions.

A. Results on $La_{0.75}Ca_{0.25}MnO_3$

LCMO25 undergoes a ferromagnetic phase transition and becomes metallic below $T_C = 190$ K.[27] To determine the dispersion of LCMO25 at large momentum transfers, we measured its ferromagnetic spin waves with incident-beam neutron energies (E_i) of 32, 50, 75, 100, 125, 150, 175, and 185 meV at $T = 8.5$ K ($0.045T_C$) on HET. The sample was oriented such that either the [1,1,0] or [0,0,1] axis of the crystal is along the incident-beam directions. For the neutron beam along the [1,1,0] axis of the crystal, we could get the dispersion relations along the $[\xi,0,0]$ or $[\xi,\xi,0]$ directions. For the neutron beam along the [0,0,1] axis, the dispersion along the $[\xi,\xi,\xi]$ direction can be obtained.

Figure 2 summarizes the spin-wave excitations for incident neutron energies of 50, 75, and 100 meV. Panels (a)–(c) show the two-dimensional color-coded contour plots of excitations in reciprocal space. Two rings of scattering are observed in these panels. The first and strongest of these two is centered at the (1,0,0) and corresponds to the intersection of the E-q region probed by the experiment and the spin-wave dispersion surface near the zone center. The second of these rings, centered at (1.5,0.5,0), corresponds to such intersections near the ZB because of a larger energy transfer E [Fig. 1(c)]. We cut the E-q data along the $[\xi,0,0]$ direction, as shown in panels (d)–(f). The cut clearly shows two distinct peaks located at 11.7 and 16.3 meV for $E_i = 50$ meV [Fig. 2(d)]. These peaks gradually disperse outward with increasing incident beam energy [Figs. 2(e) and 2(f)]. As a function of increasing energy and approaching the ZB wave vector, the spin waves become broader in width and weaker in intensity [Fig. 2(f)]. These results are consistent with our earlier measurements.[17]

To obtain spin-wave excitations along the $[\xi,\xi,0]$ direction, we change the orthogonal viewing axes of the two-dimensional spin-wave spectra and cut images along the $[\xi,\xi,0]$ direction. Figure 3 summarizes the outcome of these cuts; it is clear that the spin-wave peaks become broader and weaker near the ZB [Figs. 3(c) and 3(f)].

We systematically cut the data along all high-symmetry directions for various incident beam energies. To obtain reliable exchange coupling constant J_i's and determine their directional dependence, we analyze the data along one symmetry direction at a time with as many cuts as possible. The data are fitted simultaneously using the dynamic susceptibility $\chi''(\omega,\mathbf{q})$ described in Eq. (3) with spin-wave dispersion relation as

$$\hbar\omega_0(\mathbf{q}) = \Delta + 2S[J(0) - J(\mathbf{q})], \tag{6}$$

where Δ is the anisotropic gap and

$$J(\mathbf{q}) = \sum_i J_k e^{i\mathbf{q}\cdot(\mathbf{R}_i - \mathbf{R}_j)}. \tag{7}$$

Using the TOBYFIT nonlinear least-squares analysis program, we fit all the cuts by adjusting the peak amplitude A, damping term Γ, and magnetic exchange coupling constant J_i's. The time-of-flight measurements do not provide information at small momentum transfers, but the data obtained using triple-axis spectroscopy showed negligible anisotropic spin gap near the zone center.[10–14] We therefore fixed $\Delta = 0$ in Eq. (6) during the analysis. Following the results of our previous paper, we force J_2 and J_3 to be zero during the course of analysis, allowing only J_1 and J_4 to vary.[17] Table I shows the fitting results in LCMO25 along three major symmetry directions of $[\xi,0,0]$, $[\xi,\xi,0]$, and $[\xi,\xi,\xi]$. We note that the value of exchange constants varies in a narrow range for fitted results along different directions. For example, the NN exchange coupling J_1 changes from 7.6 to 8.4 meV, and J_4 varies from 0.26 to 0.58 meV. Using $D = \nabla_{\mathbf{q}}^2 \omega_0(\mathbf{q})|_{\mathbf{q}=0}$, where $\omega_0(\mathbf{q})$ is the dispersion relation, we can calculate the spin-wave stiffness constant D and found that $D \approx 145$ meV Å^2, consistent with the value obtained from low-q inelastic scattering measurement.[17] Since the fitting results along the three high-symmetry directions are

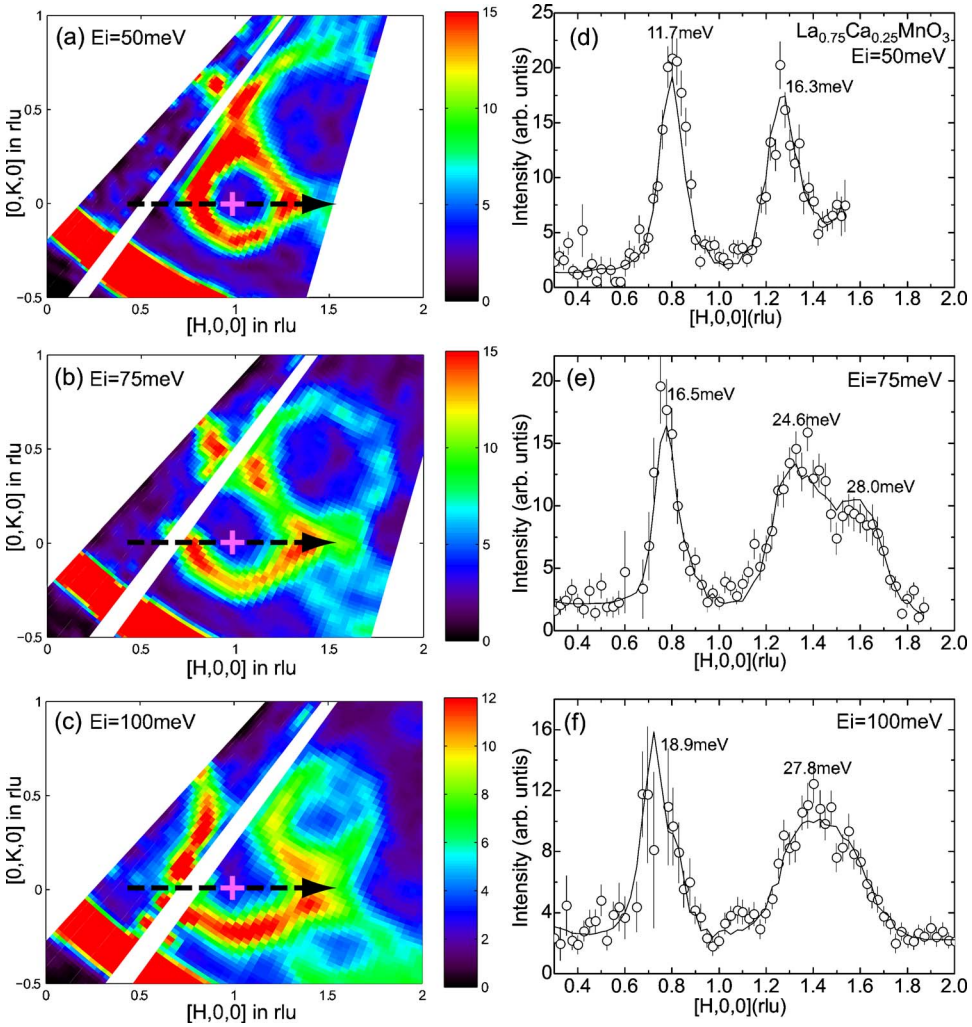

FIG. 2. (Color online) Spin-wave excitations of LCMO25 in the $[\xi,0,0]$ direction. Panels (a)–(c) illustrate the two-dimensional (2D) contour plots in the reciprocal space with incident energies of 50, 75, and 100 meV. The cross symbols indicate the FM zone center of (1,0,0). Panels (d)–(f) depict the corresponding scan profiles along the $[\xi,0,0]$ direction shown by the arrows in the left panels. The typical cut width is 0.1 rlu. Solid lines are least-squares fits using the spin-wave model described in the text. The energies associated with excitation peaks are labeled.

consistent, we included excitation data along all directions in the TOBYFIT. As shown in Table I, the global analysis with as many as 38 data sets along all directions gives $J_1=7.83\pm0.06$ and $J_4=0.51\pm0.03$ meV, which yields the ratio of $J_4/J_1=0.065\pm0.004$ and stiffness constant $D=147.2\pm2.6$ meV Å^2.

TOBYFIT gives only the fitting parameters J_i's, A, and Γ for the spin-wave dispersion relations. To actually construct a plot of E versus q of LCMO25, we derive the energy at an individual wave vector $E(q)$ by analyzing each single one-dimensional cut, as shown in Figs. 2(d)–2(f).[30] As shown in Fig. 4, the experimental data collapse nicely onto the solid line generated using Eqs. (6) and (7) with inclusion of the NN interaction J_1 and fourth NN interaction J_4. Finally, we show that a fit to a purely NN exchange coupling J_1 is not adequate. The dispersion relations based only on J_1 are plotted as the dashed lines. Although these curves describe reasonably well the low-q data, they clearly deviate the data points at the ZB with higher energies. For example, the actual ZB energies along $[\xi,0,0]$ and $[\xi,\xi,0]$ directions are 31.0 and 62.5 meV, respectively. They are lowered by about 4 and 8 meV from the prediction of the NN Heisenberg Hamiltonian. It is noted that while the description using only the NN exchange coupling is not sufficient to characterize the entire dispersion relations in LCMO25, this exchange constant J_1 is similar to the value established in the INS study of $La_{0.7}Pb_{0.3}MnO_3$.[7]

B. Results on $La_{0.7}Ca_{0.3}MnO_3$

To determine the evolution of spin-wave excitations of ferromagnetic CMR compounds, we also measured LCMO30 using HET. For these measurements, we used incident-beam energies of 50, 75, 100, 125, 150, and 185 meV. Figures 5 and 6 show raw data for LCMO30 with the same incident energies as those of LCMO25 in Figs. 2 and 3. It is clear that LCMO30 has a softened dispersion near the ZB. As shown in Fig. 5(f), the peak height at $q=[1.4,0,0]$ is only half of that at $q=[0.7,0,0]$, compared with 80% for that in LCMO25 [Fig. 2(f)]. From Eq. (4), the decrease in peak height at a similar wave vector indicates a larger damping term γ. In addition, the spin-wave ring away from (1.5,0.5,0) [Figs. 6(c) and 6(f)] collapses much faster than in LCMO25, as the incident-beam energy increases to 100 meV. Table II lists the quantitative fitting parameters using TOBYFIT. Much reduced J_1 and considerably enhanced J_4 are observed along different high-symmetry directions for LCMO30. Similar to LCMO25, the softening near the boundary shows little symmetry directional dependence.

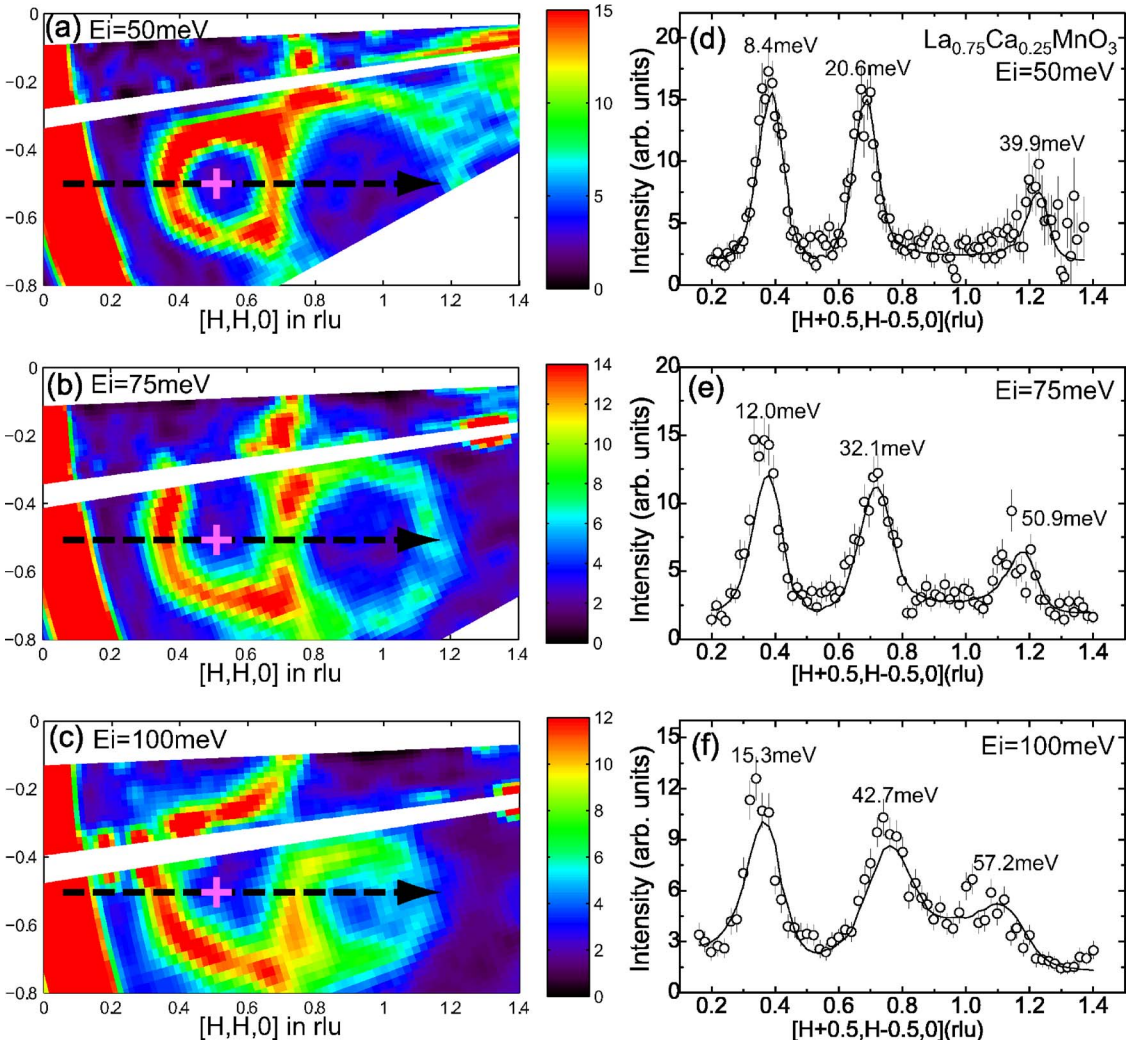

FIG. 3. (Color online) Spin-wave excitations of LCMO25 in the $[\xi,\xi,0]$ direction with incident energies of 50, 75, and 100 meV. The viewing axis of panels (a)–(c) are rotated 45° with respect to those in Fig. 2 such that the scan profiles along $[\xi,\xi,0]$ can be obtained. The cross symbols indicate the FM zone center of (1,0,0). The dashed lines depict the cutting direction.

For the global fit, we obtained $J_1=6.36\pm0.03$ and $J_4=1.24\pm0.02$ meV. The ratio of J_4/J_1 reaches 20%, a value much larger than that in LCMO25. The stiffness constant is calculated to be $D=169\pm2$meV Å^2, which agrees well with the early triple-axis scattering result.[16,31]

The dispersion curves covering the entire Brillouin zone of LCMO30 are shown in Fig. 7 with the solid lines representing the fits using J_1 and J_4, while the dashed lines represent the fits using only J_1. Inspection of Fig. 7 reveals that, as in LCMO25, the inclusion of the J_4 gives a better fit to the

TABLE I. Fitting parameters of the exchange coupling constants J_1 and J_4, the ratio of J_4/J_1, and spin-wave stiffness constant D in LCMO25. Each data set is one-dimensional scan profile, as shown in Figs. 2(d)–2(f), and consists of one or more magnetic excitation peaks. The results with only the NN interaction J_1 are listed in the last row for comparison.

Direction	J_1 (meV)	J_4 (meV)	J_4/J_1	D (meV Å^2)	No. of data sets	χ^2
$[\xi,0,0]$	7.56(7)	0.58(4)	0.076(6)	147.1±3.5	11	1.45
$[\xi,\xi,0]$	7.99(9)	0.44(4)	0.055(6)	145.6±3.9	13	1.81
$[\xi,\xi,\xi]$	8.39(14)	0.26(8)	0.032(10)	140.7±6.6	14	2.09
$[\xi,0,0]+[\xi,\xi,0]+[\xi,\xi,\xi]$	7.83(6)	0.51(3)	0.065(4)	147.2±2.6	38	1.90
$[\xi,0,0]+[\xi,\xi,0]+[\xi,\xi,\xi]$	8.75(3)	0 (fixed)	0	130.3±0.5	38	2.32

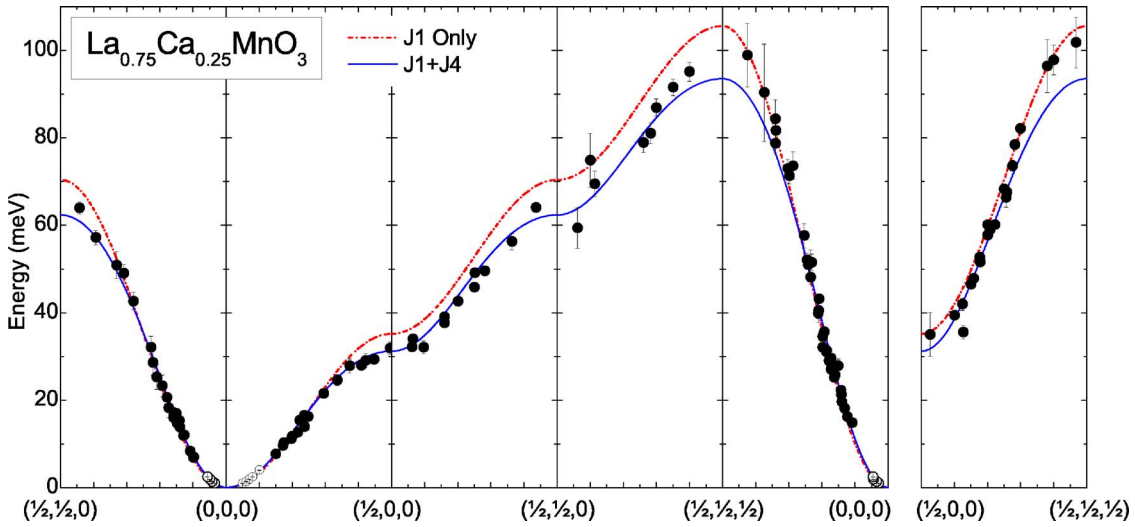

FIG. 4. (Color online) The spin-wave dispersion curves for LCMO25. The solid points are the data collected at ISIS and the open points at low energies are collected at HFIR. The dash (red) curves are the fits using only the NN interaction J_1. The solid (blue) curves are the fits combining the NN interaction J_1 and the fourth NN interaction J_4 (see text).

data. The normalized chi-squared χ^2 including J_4 is a factor of 2 less than that without it. The renormalization of spin-wave dispersions at large wave vectors is better seen in the $[\xi,0,0]$ and $[\xi,\xi,0]$ directions, where the boundary energies are lowered to 25 and 52 meV, respectively. They are nearly 9 and 15 meV lower than the expectation from a simple NN Heisenberg Hamiltonian. We note that fits at larger energies ($E>70$ meV) are not satisfactory, possibly because uncer-

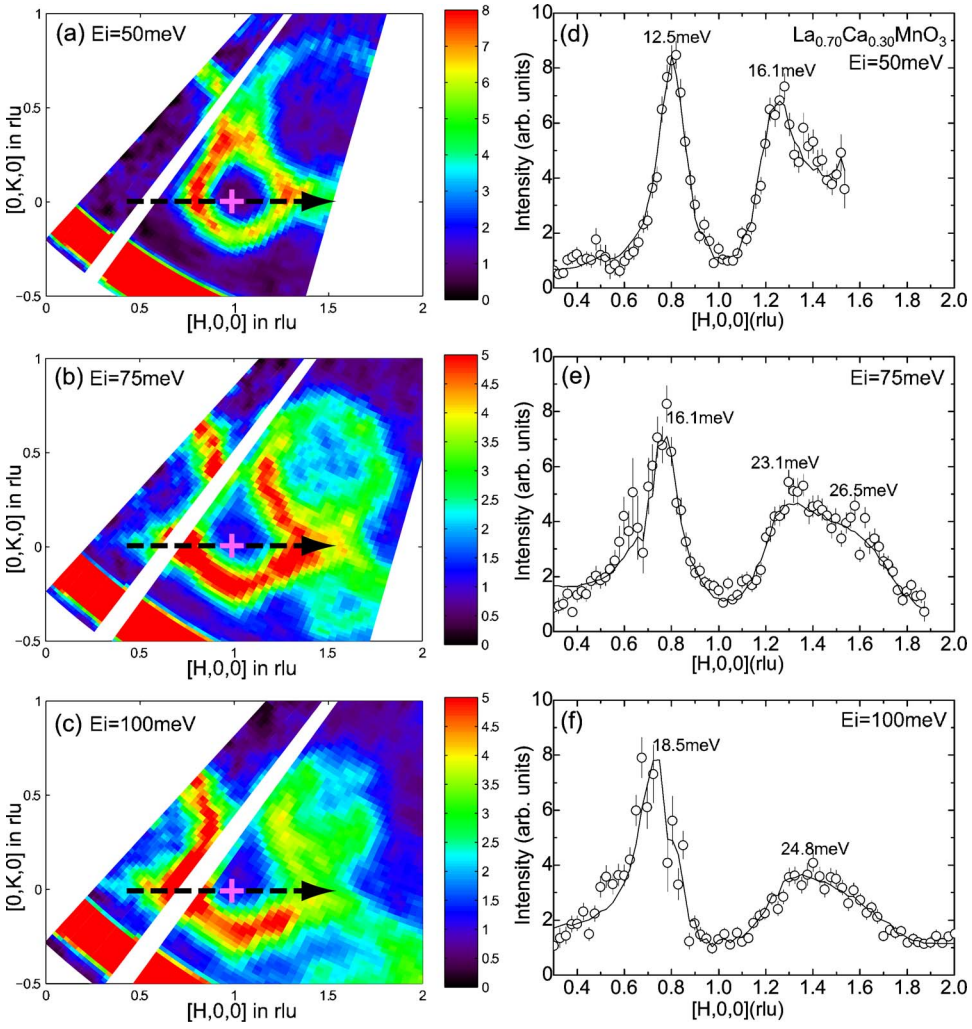

FIG. 5. (Color online) Spin-wave excitations of LCMO30 in the $[H,0,0]$ direction. Panels (a)–(c) illustrate 2D contour plots with incident energies of 50, 75, and 100 meV. Solid lines are least-squares fits (see Fig. 2 for additional information).

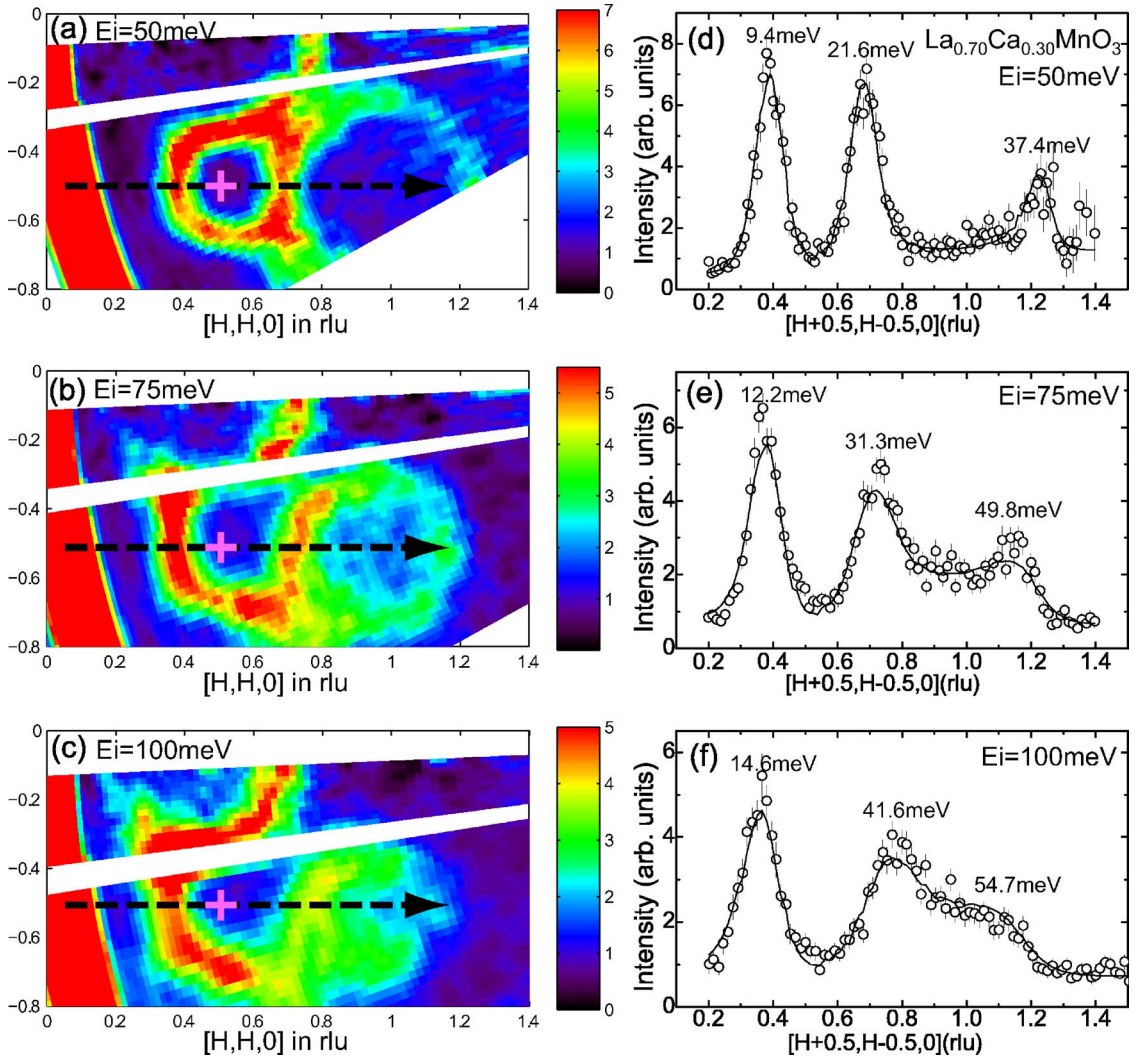

FIG. 6. (Color online) Spin-wave excitations of LCMO30 in the $[H,H,0]$ direction with incident energies of 50, 75, and 100 meV (see Fig. 2 for additional information).

tainties associated with the determination of an already damped magnetic excitation at high energies.

Having determined the dispersion relations for LCMO25 and LCMO30 using the model described in Eq. (6) with inclusion of J_1 and J_4, we now consider the other important aspect of the spin dynamics, the intrinsic width $\Gamma(\mathbf{q})$. This linewidth $\Gamma(\mathbf{q})$ is calculated from Eq. (4), where γ is obtained from the best fit to Eq. (3). It is directly associated with the relevant damping mechanisms and reflects how the quantized magnons interact with other scattering processes. The wave-vector dependence of $\Gamma(\mathbf{q})$ along with different directions is shown in Fig. 8. Note that there is a marked difference between LCMO25 and LCMO30; the widths of the latter are always larger, indicating more damped excitations in LCMO30. In addition, the momentum evolution of $\Gamma(\mathbf{q})$ does not show any anomaly across the Brillouin zone,

TABLE II. Fitting parameters of exchange coupling constants J_1 and J_4, the ratio of J_4/J_1, and spin-wave stiffness constant D in LCMO30 (see Table I for additional information).

Direction	J_1 (meV)	J_4 (meV)	J_4/J_1	D (meV Å^2)	No. of data sets	χ^2
$[\xi,0,0]$	6.01(5)	1.29(4)	0.215(8)	166.6±2.8	13	1.71
$[\xi,\xi,0]$	6.52(5)	1.18(4)	0.181(6)	167.4±2.5	22	1.91
$[\xi,\xi,\xi]$	6.56(9)	1.18(6)	0.179(11)	167.8±4.8	15	1.54
$[\xi,0,0]+[\xi,\xi,0]+[\xi,\xi,\xi]$	6.36(3)	1.24(2)	0.195(4)	168.6±1.7	50	1.74
$[\xi,0,0]+[\xi,\xi,0]+[\xi,\xi,\xi]$	8.43(3)	0 (fixed)	0	125.7±0.5	50	3.25

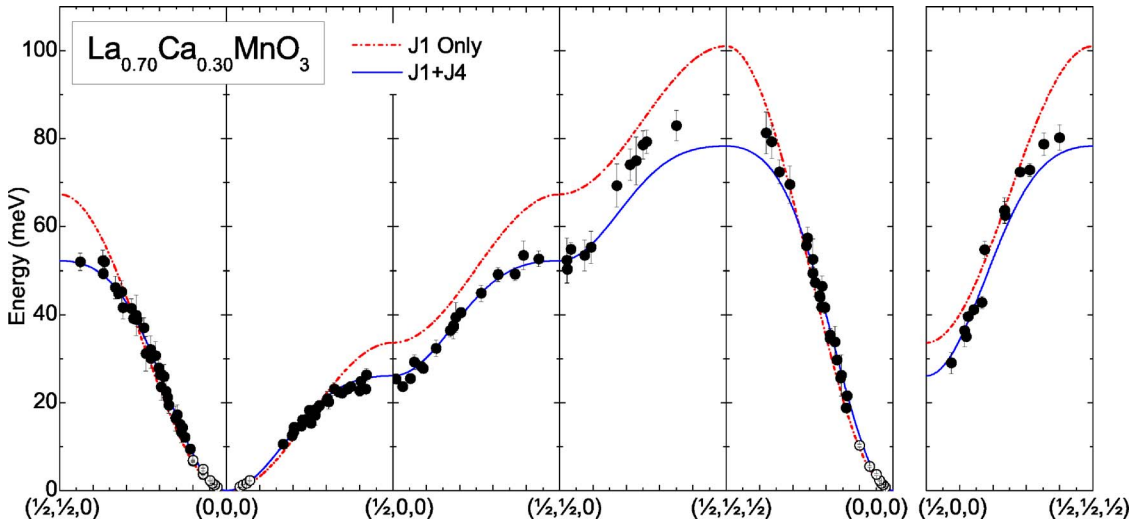

FIG. 7. (Color online) The spin-wave dispersion curves for LCMO30. The dash (red) curves are the fits using only NN interaction J_1. The solid (blue) curves are the fits using J_1 plus the fourth NN interaction J_4.

appears to be isotopic, and increases drastically near the ZB. For example, $\Gamma(\mathbf{q})$ reaches around 20 meV for E greater than 60 meV along the $[\xi,\xi,\xi]$ direction. This is unexpected from a classic, cubic Heisenberg ferromagnet, where the magnetic excitations near the ZB are well resolved.[32] The intrinsic

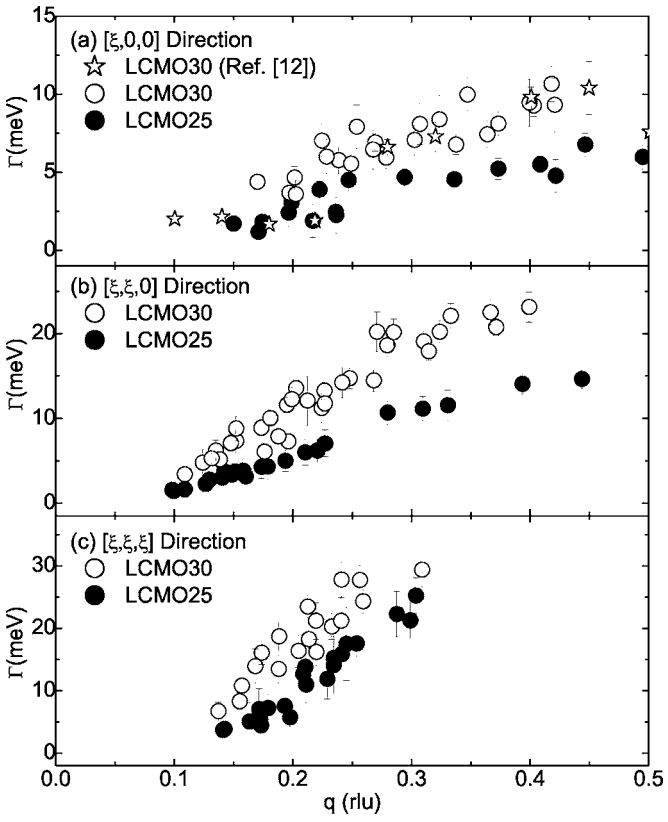

FIG. 8. The wave-vector dependence of intrinsic excitation widths $\Gamma(\mathbf{q})$ along three high-symmetry directions in LCMO25 and LCMO30. The q dependence of $\Gamma(\mathbf{q})$ along $[\xi,0,0]$ for LCMO30 obtained from triple-axis measurement (Ref. 12) is displayed for comparison.

widths in both LCMO25 and LCMO30 are much broader, indicating that one or more decay mechanisms play an important role in these CMR compounds.

We are now in a position to compare our data to various possible mechanisms of the ZB softening. First, we want to comment on the role of disorder or randomness which is naturally present in these compounds. Motome and Furukawa[23] have pointed out that disorder in CMR materials will cause anomalous broadening and/or anticrossing in the spin excitation spectra. In this scenario, the one-electron bandwidth is proportional to the average ionic size at La/Ca site ($\bar{r}=\Sigma_i x_i r$, where x_i is the fractional occupancies of A-site species and r_i is the individual radius). In a previous paper, we have characterized the softening of dispersion relation in a series of doped manganites near $x=0.30$ along the $[\xi,0,0]$ direction.[17] We found that the renormalization near ZB has little dependence on the average ionic size at A site. For LCMO25 and LCMO30, $\bar{r}$ becomes 1.207 and 1.205 Å, respectively, showing very little variation of oxygen octahedron distortion surrounding the Mn ions. On the other hand, the mismatch between La and Ca ions will cause a quenched disorder in the system, which can be qualitatively characterized by $\sigma^2=\Sigma_i(x_i r_i^2-\bar{r}^2)$.[33,34] Based on this, σ^2 is 2.43×10^{-4} for LCMO25 and 2.72×10^{-4} for LCMO30. Clearly, the differences in quenched disorder between LCMO25 and LCMO30 are rather small and cannot account for the dramatic change of spin-wave spectra near the ZB. We therefore conclude that the disorder effect does not play an important role in this doping range of LCMO.

Second, the effect of magnon-phonon coupling may be the microscopic origin of the observed magnon broadening and damping. Dai *et al.* suggested that the interaction between optical phonon and spin-wave branches may lead to the broadening of spin-wave spectrum in a number of doped manganites near $x=0.30$.[12] In this picture, a dispersionless optical phonon branch with energy around 20 meV goes across the whole Brillouin zone and interacts with the magnon branch, causing softening and a substantial increase of the magnetic excitation linewidths. The measurements of Dai

et al. were carried out with unpolarized neutrons, and it was difficult to separate the magnetic scattering from the purely lattice excitations. Recent measurements by Fernandez-Baca *et al.*[35] using polarized-neutron-scattering techniques confirmed that the ZB spin waves of LCMO30 in the $[\xi,0,0]$ and $[\xi,\xi,0]$ directions are considerably broad and have energies lower than those expected from the approximation to the NN Heisenberg Hamiltonian, although the softening in $[\xi,\xi,0]$ is less severe than originally reported.[36] While the magnon-phonon interaction mechanism seems to explain the broadening of the spin waves, it is not clear if it would fully account for the magnitude of the observed softening in LCMO30 at the zone boundary. Furthermore, this mechanism may not be relevant to the general case of the manganites as the observed spin waves in the $Sm_{0.55}Sr_{0.45}MnO_3$ are softened to around 15 meV (which is below the 20 meV optical phonon) at the ZB along the $[\xi,0,0]$ direction, with no evidence of broadening.[22]

Finally, the distinct feature of ZB softening might be a consequence of the e_g-band filling in the half-metallic region.[19] Solovyev and Terakura suggested that the canonical double exchange is no longer appropriate as soon as holes are doped into the system. Longer range FM interactions lead to the softening at the zone boundary and contribute to the increase of the stiffness constant D.[19] However, the details of the realistic electronic structure are important and may significantly modify the analysis, particularly if the effects of t_{2g} electrons are taken into account. For example, the x dependence of magnetic interactions is substantially modified by the change of DE interaction contributed by t_{2g} electrons and D might even decrease with x. Such complex scenario prevents us from making meaningful comparison with D's yield experimentally. It is also unclear whether this model can explain the commonly observed damping and/or broadening of magnetic excitation near the ZB. We would like to point out that, in the tight-binding approximation used by these authors, only the exchange couplings along the Mn-O-Mn chain (J_1, J_4, J_8, and J_{15} as defined in Ref. 19) would bring appreciable contributions to the spin-wave dynamics. Our work and that of Endoh *et al.*[22] show that J_1 and J_4 are the only exchange constants contributing to the ZB softening. There is close correlation between J_i's and the orbital polarized states;[22] J_2 would be enhanced by (x^2-y^2)-type orbitals and J_4 is enhanced by $(3z^2-r^2)$-type orbitals. It is surprising that a large increase of J_4/J_1 occurs despite the small change in nominal hole doping. This might indicate a drastic modification of (preformed) orbital correlations which favor the overlap between neighboring Mn ions.[37] We hope that the results presented here will help to stimulate further experimental and theoretical investigations, leading to a complete understanding of the magnetic dynamics in those CMR materials.

IV. CONCLUSIONS

In summary, we have performed a systematic study on the spin-wave dynamics in the CMR manganites LCMO25 and LCMO30 using inelastic-neutron-scattering techniques. We find that both systems display considerable spin-wave renormalization along all high-symmetry directions. Consistent with early measurements, which entirely focus on the [1,0,0] direction, we find that the dispersion relations can be phenomenologically analyzed using the NN interaction J_1 and the fourth NN interaction J_4. The introduction of J_4 lowers J_1 and therefore lowers the ZB energy. As a result of this, the systems with a larger J_4/J_1 ratio exhibit a larger SW softening at the ZB. The possible mechanisms responsible for such boundary softening are also discussed.

ACKNOWLEDGMENTS

We thank Thomas Enck for preliminary data analysis. The authors are grateful for the valuable discussion with M. E. Hagen. This work was supported by the U.S. NSF under Grant No. DMR-0453804. Oak Ridge National Laboratory is managed by UT/Battelle, LLC, for the U.S. Department of Energy under Contract No. DE-AC05-00OR22725.

*Electronic address: yef1@ornl.gov

[1] M. B. Salamon and M. Jaime, Rev. Mod. Phys. **73**, 583 (2001).
[2] Y. Tokura, *Colossal Magnetoresistive Oxides* (Gordon and Breach Science, New York, 2000).
[3] E. Dagotto, T. Hotta, and A. Moreo, Phys. Rep. **344**, 1 (2002).
[4] C. Zener, Phys. Rev. **82**, 403 (1951).
[5] N. Furukawa, J. Phys. Soc. Jpn. **65**, 1174 (1996).
[6] M. C. Martin, G. Shirane, Y. Endoh, K. Hirota, Y. Moritomo, and Y. Tokura, Phys. Rev. B **53**, 14285 (1996).
[7] T. G. Perring, G. Aeppli, S. M. Hayden, S. A. Carter, J. P. Remeika, and S.-W. Cheong, Phys. Rev. Lett. **77**, 711 (1996).
[8] Y. Endoh and K. Hirota, J. Phys. Soc. Jpn. **66**, 2264 (1997).
[9] Y. Motome and N. Furukawa, Phys. Rev. B **68**, 144432 (2003).
[10] H. Y. Hwang, P. Dai, S.-W. Cheong, G. Aeppli, D. A. Tennant, and H. A. Mook, Phys. Rev. Lett. **80**, 1316 (1998).
[11] L. Vasiliu-Doloc, J. W. Lynn, A. H. Moudden, A. M. de Leon-Guevara, and A. Revcolevschi, Phys. Rev. B **58**, 14913 (1998).
[12] P. Dai, H. Y. Hwang, J. Zhang, J. A. Fernandez-Baca, S.-W. Cheong, C. Kloc, Y. Tomioka, and Y. Tokura, Phys. Rev. B **61**, 9553 (2000).
[13] T. Chatterji, L. P. Regnault, and W. Schmidt, Phys. Rev. B **66**, 214408 (2002).
[14] F. Moussa, M. Hennion, F. Wang, P. Kober, J. Rodriguez-Carvajal, P. Reutler, L. Pinsard, and A. Revcolevschi, Phys. Rev. B **67**, 214430 (2003).
[15] J. A. Fernandez-Baca, P. Dai, H. Y. Hwang, C. Kloc, and S.-W. Cheong, Phys. Rev. Lett. **80**, 4012 (1998).
[16] P. Dai, J. A. Fernandez-Baca, E. W. Plummer, Y. Tomioka, and Y. Tokura, Phys. Rev. B **64**, 224429 (2001).
[17] F. Ye, P. Dai, J. A. Fernandez-Baca, H. Sha, J. W. Lynn, H. Kawano-Furukawa, Y. Tomioka, Y. Tokura, and J. Zhang, Phys. Rev. Lett. **96**, 047204 (2006).

[18] D. I. Golosov, Phys. Rev. B **71**, 014428 (2005).
[19] I. V. Solovyev and K. Terakura, Phys. Rev. Lett. **82**, 2959 (1999).
[20] G. Khaliullin and R. Kilian, Phys. Rev. B **61**, 3494 (2000).
[21] S. Krivenko, A. Yaresko, G. Khaliullin, and H. Fehske, J. Magn. Magn. Mater. **272-276**, 458 (2004).
[22] Y. Endoh, H. Hiraka, Y. Tomioka, Y. Tokura, N. Nagaosa, and T. Fujiwara, Phys. Rev. Lett. **94**, 017206 (2005).
[23] Y. Motome and N. Furukawa, J. Phys. Soc. Jpn. **7**, 1, 1419 (2002); **72**, 472 (2003).
[24] Y. Motome and N. Furukawa, Phys. Rev. B **71**, 014446 (2005).
[25] X. Wang, Phys. Rev. B **57**, 7427 (1998).
[26] T. A. Kaplan, S. D. Mahanti, and Y.-S. Su, Phys. Rev. Lett. **86**, 3634 (2001).
[27] P. Dai, J. A. Fernandez-Baca, N. Wakabayashi, E. W. Plummer, Y. Tomioka, and Y. Tokura, Phys. Rev. Lett. **85**, 2553 (2000).
[28] R. Coldea, MSLICE, a data analysis program for time-of-flight neutron spectrometers, 2004.
[29] T. G. Perring, TOBYFIT, least-squares fitting to single-crystal data on HET, MARI, and MAPS, 2004.
[30] In this approach, only J_1 is allowed to vary (the amplitude A is fixed as its value has already been reliably determined from the global fitting and J_4 is fixed to be zero); the analysis would not carry the collective information of the whole dispersion relation but does provide the correct energy at a specific wave vector q.
[31] J. W. Lynn, R. W. Erwin, J. A. Borchers, Q. Huang, A. Santoro, J.-L. Peng, and Z. Y. Li, Phys. Rev. Lett. **76**, 4046 (1996).
[32] For instance, neutron-scattering measurements on the prototype Heisenberg ferromagnet EuO show that the magnons broadening is small even at the zone boundary. H. A. Mook and J. A. Fernandez-Baca (unpublished).
[33] L. M. Rodriguez-Martinez and J. P. Attfield, Phys. Rev. B **54**, R15622 (1996).
[34] R. D. Shannon, Acta Crystallogr., Sect. A: Cryst. Phys., Diffr., Theor. Gen. Crystallogr. **32**, 751 (1976).
[35] J. A. Fernandez-Baca, M. E. Hagen, P. Dai, F. Ye, J. Kulda, Y. Tomioka, and Y. Tokura, Physica B **385-386**, 66 (2006).
[36] The ZB magnon energy in the $[\xi,\xi,0]$ direction of 52 meV reported from our unpolarized neutron experiments is in agreement with the value 53 ± 2 meV measured by Fernandez-Baca *et al.*, with polarized neutrons (Ref. 35). The reason for this agreement is attributed to the fact that using an incident energy of 100 meV allowed us to measure the magnons in the (1,0,0) Brillouin zone, where the magnetic scattering dominates the measured spectra.
[37] The possibility of the ordering of complex orbitals in the ferromagnetic metallic manganites has been discussed by van den Brink and D. Khomskii. This type of orbital ordering would not introduce any lattice distortions and would preserve the essentially cubic symmetry of these materials. See, for example, J. van den Brink and D. Khomskii, Phys. Rev. B **63**, 140416(R) (2001).